High-coordinated Bi^V/Bi^{IV} regulates photocatalytic selective activation of structural oxygen and self-generated H_2O_2 dominating an efficient synergistic sterilization

Qiyu Lian [a], Zhuocheng Liang [a], Xinyi Guan [a], Zhuoyun Tang [a], Rumeng Zhang [a], Boyi Yang [a], Yingxin Wu [a], Huinan Zhao [a], Chun He [a,b], Dehua Xia [a,b,*]

[a] *School of Environmental Science and Engineering, Sun Yat-Sen University, Guangzhou 510275, China*
[b] *Guangdong Provincial Key Laboratory of Environmental Pollution Control and Remediation Technology, Guangzhou 510275, China*

ARTICLE INFO

ABSTRACT

This study revealed that the high-coordinated Bi^V/Bi^{IV} regulates the photocatalytic selective activation of structural oxygen (O_{lat}/O_{ads}) and self-generated H_2O_2 assisted by the multi-physical-like effects enabling the efficient synergistic sterilization. Explicitly, we designed a new antibacterial material, α-Bi_2O_{3-x}@PPy, that functions the physical assembly and photothermal effects accomplishing the physical-like pre-damage to the cell membrane by completely unbolting its permeability, which greatly boosts the fatal bacterial inactivation achieved by the photocatalytic selective reactions. More importantly, this work found that the specific high-coordinated Bi^V/Bi^{IV}, generated via Bi-C-N bonds, regulates the selective $\bullet O_2$ generation with 80% selectivity by the photocatalytic activation of the adjacent O_{lat}/O_{ads} and simultaneously, triggers the self-generated H_2O_2 activation to produce hydroxide radicals ($\bullet OH$), thus forming the dominant oxidation assaults for the fatal bacterial inactivation. Conclusively, this study not only enriches the fundamental principles for photocatalytic selective reaction but also provides a candidate sterilization strategy for practice applications.

1. Introduction

Currently, the sterilization strategies of the mutual physic-chemical effects accomplished by the multi-functional antibacterial materials have arisen from the great sterilization performance [1–3]. And, the mainstream perspectives believe that the synergistical sterilization strategies are more likely attributed to the chemical effects that cause oxidative stress initiated by either reactive oxygen species (ROS) or electrons transfer than the physical effects as the assistant role that wound the cell membranes by the sharp edges with either parallel or perpendicular interaction modes, but not achievable without either physical or chemical effects [4–7]. Therefore, the physical effects have been claimed to be the necessary and key assistants to open the channel by breaking the cell wall for further promoting the fatal oxidative assault towards the metabolic functions of bacteria [6,8,9]. Usually, an advanced antibacterial material capable of the synergistic physic-chemical effects requires the specific morphology, structure, or surface properties, such as ultrathin graphene-like nanosheets with the sharp edges or the specific functional surface, but it is also constrained

by the low stability, high cost, synthesis complication, and simultaneously manipulating oxidative stress for the practical sterilization [10–14]. Thus, to not be limited by these constraints, a novel idea to design and develop the advanced antibacterial material is needed.

Except for damaging the cell membrane via sharp edges, the photothermal effects pave a new pathway to accomplish the physical-like effects in the antibacterial activities without requiring the unique morphology or surface for the antibacterial materials. Many studies have claimed that the photothermal assaults could effectively cause the thermal denaturation of proteins or thermo-mechanical damage onto the cell membrane, which are extensively applied in the field of biological therapy [15,16]. For instance, Mackey and coworkers declared the occurrence of irreversible thermal denaturation for Escherichia coli and Bacillus stearothermophilus at 51 ℃ [17]. Qin and Bischof comprehensively summarized the photothermal effects attributed to the surface plasmon resonance (SPR) of gold nanoparticles onto the biological responses of cell membrane, proteins, DNA, and other bio-macromolecules [18]. Especially, our team recently reported that the photothermal effects by Au/TPR can cause the physical-like damage

to the outer bacterial membrane and avail the ROS attack to the intra-cellular cytoplasm [19]. Thus, we see that the photothermal effects are capable of the physical-like damage of bacterial membrane, which greatly benefits the catalytic oxidative assaults for the fatal bacterial inactivation.

Beyond the assistant physical-like damage, the fatal oxidative assaults play the more important role in the sterilization performance. Usually, the way that selectively generates the single ROS can avoid the rate-determined reaction steps and significantly enhance the ROS mass transfer efficiency, which is more preferential for the water remediation [20]. As reported, the Fe_1/CN catalyst containing uniform $Fe-N_4$ sites achieves the generation of $^1O_2$ with 100% selectivity by activating peroxymonosulfate enabling the ultrafast degradation of p-chlorophenol in water [15,21]. Heuristically, the selective generation of a single ROS as the primary oxidative assaulter might be a new sterilization strategy by designing the novel antibacterial material to achieve the efficient sterilization performance. But, accomplishing the selective generation of single ROS over the antibacterial material is not an easy task, which is mainly constrained by modulating the specific active sites on the catalysts. Beyond this, a new emerged strategy that constructs high-coordinated metal sites can efficiently trigger the selective generation of oxidative species. For instance, the Fe^{IV}/Fe^V active sites can selectively produce the $Fe^{IV}=O/Fe^V=O$ species by activating H_2O_2 for the efficient oxidation reactions [22]. Besides, the Fe sites in hetero-metallic Ti_4Fe_1 cocrystal promote the selective production of $^1O_2$ by activating O_2 for the efficient $C(sp^3)$-H bond activation [23]. Inspired by these studies, we select the bismuth (Bi) to construct the high-coordinated Bi^V/Bi^{IV} sites for the selective generation of reactive species, because Bi is well-known by its broaden covalence range and widely optical and bio-medicinal applications [24–26], as well as the high reactive activity of Bi^V/Bi^{IV}, which could be the potential candidate for designing the novel antibacterial material with selectivity. Therefore, designing a novel antibacterial material that simultaneously possesses the high-coordinated Bi^V/Bi^{IV} sites and the photothermal property is the main task to be solved in this study.

Inspiringly, the recent study reported the electron delocalization can induce the high-coordinated Ni formation by the $Ni-N_4$ structure in the NiO complexed Ni-N-C catalyst [27,28]. Thus, this study could provide a new approach to construct the high-coordinated Bi^V/Bi^{IV} sites by complexing BiO_x with N-C based materials. Polypyrrole (PPy), a familiar N-C based material, is extensively acknowledged by its economical character, photothermal ability, high electrical conductivity, and antibacterial property, which appropriately satisfies our needs to design the new antibacterial material in this study [29,30]. So herein, we exploratorily complexed the reduced α-Bi_2O_{3-x} with PPy to synthesize the desired antibacterial material of α-Bi_2O_{3-x} @PPy and successfully applied it in the sterilization evaluation. The experimental results manifested that the α-Bi_2O_{3-x} @PPy behaves a bacterial adhesion property and the significantly enhanced photothermal physical-like effects resulting in the physical-like damage towards the cell membrane, which benefits the further fatal oxidative assaults towards bacteria. Besides, the α-Bi_2O_{3-x} @PPy also possesses the abundant high-coordinated Bi^V/Bi^{IV} active sites that function the selective photocatalytic generation of abundant $\bullet O_2^-$ and the activation of self-generated H_2O_2 via the two-electron O_2 reduction on the PPy components to produce $\bullet OH$, which acts as the fatal oxidative assaults towards the bacteria. So conclusively, this work not only designs a new antibacterial material but also provides a new candidate strategy that mutually combines the photothermal physical-like effects and the selective oxidations for the enhanced sterilization.

2. Experimental

2.1. Preparation of α-Bi_2O_{3-x}

The α-Bi_2O_{3-x} was prepared by a reported method [31]. Firstly, 2.0 g

$Bi(NO_3)_3 \cdot 5 H_2O$ was dissolved in the 1 M HNO_3 solution. Then, 0.1 g hexadecy trimethy ammonium bromide (CTAB), as a cation surfactant, was added into the solution to improve the degree of crystallinity under continuous stirring [32]. Next, 20 mL DI water that dissolved 8.4 g NaOH was dropwise added the foregoing mixture at 60 ℃ under continuous stirring for 30 min. Next, the mixture was washed by DI water and dried in air at 60 ℃ overnight, followed by the calcination at 350 ℃ for 2 h to obtain a-Bi_2O_3. Beyond, 0.466 g as-prepared a-Bi_2O_3 was added into the 100 mL DI water that dissolved 1.0 g poly-vinylpyrrolidone K90 (PVP), which can help to control the formation of the nanostructure and morphology of α-Bi_2O_{3-x} [33], under continuous stirring for 1 h. Then, 22.70 mg $NaBH_4$ solution was dropwise added into the mixture. Finally, the mixture was washed by ethanol and DI water for several times, and then dried in air at 60 ℃ overnight to obtain the final product of α-Bi_2O_{3-x}.

2.2. Preparation of α-Bi_2O_{3-x} @PPy

Typically, 0.10 g of as-prepared α-Bi_2O_{3-x} and 1.14 g of P-TSA were dispersed in 30 mL of deionized (DI) water under ultrasonication. Then, the suspension was transferred into ice bath under violent stirring and cooled down to below 5 °C. Subsequently, 66.7 µL of pyrrole monomer was dropped into the above suspension and stirred for 30 min, followed by the addition of Ammonium persulfate (APS) solution (0.11 g APS dissolved in 10 mL DI water). The mixture was stirred for at least 6 h under ice bath condition. Finally, the α-Bi_2O_{3-x} @PPy product was collected by filtration and washed for three times, and then dried at 60 °C under vacuum for 24 h. The α-Bi_2O_{3-x} @PPy composites with various proportion (wt%) of PPy were fabricated by varying the dosage of pyrrole monomer as 400, 150, and 66.7 µL. which were denoted as α-Bi_2O_{3-x} @PPy-400, α-Bi_2O_{3-x} @PPy-150, and α-Bi_2O_{3-x} @PPy-66.7, respectively.

The sections of the chemicals, characterization, sterilization tests, analysis methodology, and theoretical calculation were placed in the supporting information (S1.1-S1.7).

2.3. Characterization of materials

X-ray diffraction (XRD) analysis was obtained by using a D/max 2200 PC diffractometer (RIGAKU, Japan) equipped with Cu Kα radiation on range from $10.0°-80.0°$. The morphology was observed using a Quanta 400 F thermal field emission scanning electron microscopy (SEM, Shimazhu, Japan). Additionally, the energy-dispersive spectroscopy (EDS) and mapping analysis was collected by the EDAX Gensis EDS spectrometer, which was compatible with SEM. The UV–vis–NIR absorption spectra were measured by a Lambda 950 UV–vis–NIR spectrophotometer (PerkinElmer, US). To evaluate the photothermal property of α-Bi_2O_3, α-Bi_2O_{3-x}, and α-Bi_2O_{3-x} @PPy, the interfacial temperature was measured by a submerged thermocouple microprobe and a thermal camera (226 s, Fotric, US) for obtaining thermal images. Besides, the electrochemical tests were introduced to measure the photoelectrochemical performance of α-Bi_2O_3, α-Bi_2O_{3-x}, and α-Bi_2O_{3-x} @PPy by using CHI 660E electrochemical workstation. The three-electrode quartz cells system was equipped with a saturated calomel electrode (SCE) serving as a reference electrode, Pt plate as a counter electrode and stainless steel coated with α-Bi_2O_3, α-Bi_2O_{3-x}, and α-Bi_2O_{3-x} @PPy as working electrodes while the electrolyte was 1 mol/L Na_2SO_4 solution. Aimed at examining the property of photothermal conversion of as-prepared catalysts, the temperature elevation in the batch reactor under irradiation was recorded by a submerged thermocouple microprobe. To examine the ROS that played major roles in the process, electron spin resonance (ESR) spectra were introduced via a JES FA200 spectrometer. 5,5-dimethyl-1-pyrroline N-oxide (DMPO) was implied as the trapping agent for the determination of $\bullet OH$ and $\bullet O_2^-$ (methanol solvent for DMPO-$\bullet O_2^-$ and aqueous solvent for DMPO-$\bullet OH$), when 2,2,6,6-Tetramethylpiperidine (TEMP) was used to trap $^1O_2$.

2.4. Sterilization tests

E. coli K-12 was used as representative bacteria to evaluate the sterilization activities of as-prepared α-Bi$_2$O$_{3-x}$@PPy. *E. coli K-12* cells were first cultured in nutrient broth (NB) at 37 °C for 16 h. Then, an appropriate amount of bacteria were collected and washed twice using sterilized water to produce a cell density of 10^8 cfu/mL. In the sterilization experiments, 25 mg of as-prepared materials and 0.25 mL of the above bacterial suspension were added into 25 mL of sterilized water/ 100 mM H$_2$O$_2$ to achieve the initial cell density of 10^7 cfu/mL. A 300 W xenon lamp (PLS-SXE300) with a 420 nm cut-off filter was used to provide vis-IR irradiation. In each pre-set time interval, the collected bacterial samples were quickly spread on the agar plate and incubated overnight at 37 °C to count the bacterial cell density. All the experiments were repeated for three times.

2.5. Analysis

2.5.1. Cell membrane damage

(a) The bacterial samples before and after treatment were collected and subsequently stained with a LIVE/DEAD BacLight Bacterial Viability Kit (Molecular Probes, USA), then observed with a fluorescence microscope; (b) The changes in the bacterial morphology were observed by SEM (Joel-JSM-6301-F). (c) Cell permeability assay: O-nitrophenyl β-D-galactopyranoside (ONPG), a specific substrate of β-D-galactosidase, will be hydrolyzed to o-nitrophenyl which is yellow and can be determined by colorimetric method under the action of enzyme catalysis; (d) MDA Assay kit was used to detect Malondialdehyde (MDA) whose content reflects the degree of lipid peroxidation in the cell during the photothermal antibacterial process.

2.5.2. Fluorescence-based staining tests

Considering that the microscopic observation has a delay, the fluorescence-based cell staining test was used to identify the instant destruction of cell membranes with PI and SYTO 9 as fluorescence probes. After being treated by a Live/Dead Baclight Bacterial Viability Kit (L7012, Thermofisher Scientific, US), bacterial samples were observed via laser scanning fluorescence microscopy (Olympus, FV1000) and CytoFLEX flow cytometer (Beckman, US).

2.5.3. Intracellular antioxidant enzyme activity

(a) GSHPX Assay kit was used to extract glutathione (GSH) which is an important intracellular antioxidant enzyme, and the loss of GSH was assessed by measuring the absorbance at 630 nm (colorimetric method); (b) Catalase (CAT) activity in the supernatants was tested with the Assay Kit.

2.6. H$_2$O$_2$ production measurement

The H$_2$O$_2$ concentration was determined by the 4-Amino-N, N-diethylaniline sulfate salt (DPD)-Peroxidase (POD) method. Different gases were firstly bubbled into the reaction system for 30 min to ensure adsorption-desorption equilibrium in the dark. During reaction processes (0.2 mg/mL for catalysts) under irradiation, 1.5 mL of the mixture was sampled at regular intervals and filtered with a 0.22 μm filter. 1 mL of samples were mixed with 3 mL of PBS buffer (pH = 6, 0.2 M) and 5.9 mL DI water, followed by the addition of 50 μL DPD and 50 μL POD. After shaking and 50-s standing, the absorbance at OD$_{551}$ was recorded by a UV–vis spectrophotometer.

3. Results and discussions

3.1. The evaluation of sterilization performance

We firstly evaluated the sterilization performance on the α-Bi$_2$O$_{3-x}$@PPy under visible-infrared (vis-NIR) irradiation (298.2 mW cm^{-2}).

The disinfection experiments were conducted at an initial *Escherichia coli (E. coli)* K-12 cell density of $10^{6.5}$ colony-forming units (cfu)/mL. In Fig. 1**a**, the bare exposure to visible-infrared irradiation has almost no sterilization performance towards *E. coli* K-12. While the α-Bi$_2$O$_{3-x}$@PPy behaves the extradentary sterilization performance for *E. coli* K-12 of 6.11 log$_{10}$cfu/mL within 30 min at the same condition. Besides, the α-Bi$_2$O$_{3-x}$@PPy still behaves a similar performance when the volume of reaction system was enlarged by 10 times into 250 mL at the same condition (Fig. S1), confirming the great sterilization activity of α-Bi$_2$O$_{3-x}$@PPy. In contrast, the PPy, α-Bi$_2$O$_3$, and α-Bi$_2$O$_{3-x}$ only accomplish inactivating *E. coli* K-12 of 1.62、2.58、3.91 log$_{10}$cfu/mL, respectively. Additionally, the stability of α-Bi$_2$O$_{3-x}$@PPy was also evaluated and shown in Fig. S2. The results demonstrate that the α-Bi$_2$O$_{3-x}$@PPy still accomplishes inactivating *E. coli* K-12 of average 6.02 log$_{10}$cfu/mL after the continuous 4 cycles indicating a great stability for the synergistic sterilization. Encouraged by the great sterilization performance of α-Bi$_2$O$_{3-x}$@PPy under vis-NIR irradiation, we further investigated the unique role of physical effects and oxidative assaults in the contribution to the great sterilization performance. Particularly, the α-Bi$_2$O$_{3-x}$@PPy/vis-NIR system was found to be greatly superior in contrast to either bare photocatalytic system or bare thermal system, as the reference systems, in terms of sterilization performance, and the bare thermal physical-like effects behaved a remarkable sterilization performance of 3.58 log10cfu/mL within 30 min and 6.11 log$_{10}$cfu/mL within 60 min (Fig. 1**b**), much better than bare photocatalytic system. This phenomenon points out the potential unique thermal physical-like effects on the sterilization performance in the α-Bi$_2$O$_{3-x}$@PPy/vis-NIR system. In another aspect, the α-Bi$_2$O$_{3-x}$@PPy/vis-NIR system behaved the significantly higher than the sum of bare photocatalytic system and thermal system in terms of the number of inactivated *E. coli* K-12 at the same contact time. Besides, this system also exhibits a great sterilization performance for the other pathogens like *Spingopyxis sp.* BM1–1 fungus and MS2 virus usually existing in the natural waterbodies (Fig. 1**c**). Therefore, these results confirmed that the thermal physical-like effects and the fatal oxidative assaults could synergistically contribute to the greatly efficient sterilization performance.

3.2. Exploring the multiple assaults for the sterilization performance

To probe the insights into the great sterilization performance in the α-Bi$_2$O$_{3-x}$@PPy/vis-NIR system, the mutual physical-like damage to the cell membrane of *E. coli* K-12 was investigated. Firstly, the characterization of α-Bi$_2$O$_{3-x}$@PPy was investigated to well understand its surficial structure and properties. The α-Bi$_2$O$_{3-x}$@PPy (Fig. 1**d**) shows the same primary characteristic peaks at $2\theta = 24.66–35.17°$ corresponding to the crystal facets family of {120} [34] with the original α-Bi$_2$O$_3$ and α-Bi$_2$O$_{3-x}$ standard cards (PDF# No.72–0398), consistent with the TEM results that the α-Bi$_2$O$_{3-x}$ and α-Bi$_2$O$_{3-x}$@PPy microrods primarily expose the (102) facet belonging to {120} (Fig. S3). Additionally, the EDS results show that the elements Bi and O are the primary contents and only 0.33 wt% of N (Fig. S4) is observed indicating that no other impurities are remained on the surface of α-Bi$_2$O$_{3-x}$. These phenomenon indicates that the characteristic structure of α-Bi$_2$O$_{3-x}$ was greatly retained in the α-Bi$_2$O$_{3-x}$@PPy [35]. The morphology of α-Bi$_2$O$_{3-x}$@PPy was clarified by the TEM (Fig. S3) and SEM (Fig. S5) results that the α-Bi$_2$O$_{3-x}$@PPy microrods with a size of 10–20 μm was formed by integrating the amorphous PPy onto the crystal α-Bi$_2$O$_{3-x}$, which apparently distinguishes from the α-Bi$_2$O$_3$ and α-Bi$_2$O$_{3-x}$ microrods. Besides, it was found that the α-Bi$_2$O$_{3-x}$@PPy is roughly comprised of 70% of α-Bi$_2$O$_{3-x}$ and 30% of PPy in terms of mass proportion from TGA results (Fig. S6).

Therefore, the specific morphology of the α-Bi$_2$O$_{3-x}$@PPy with rough surface (Fig. S3 and S4) will be greatly conducive to catch the bacteria via the physical electrostatic attraction. As shown in Fig. 1**e**, the positive-charged surface of α-Bi$_2$O$_{3-x}$@PPy was apparently enhanced in
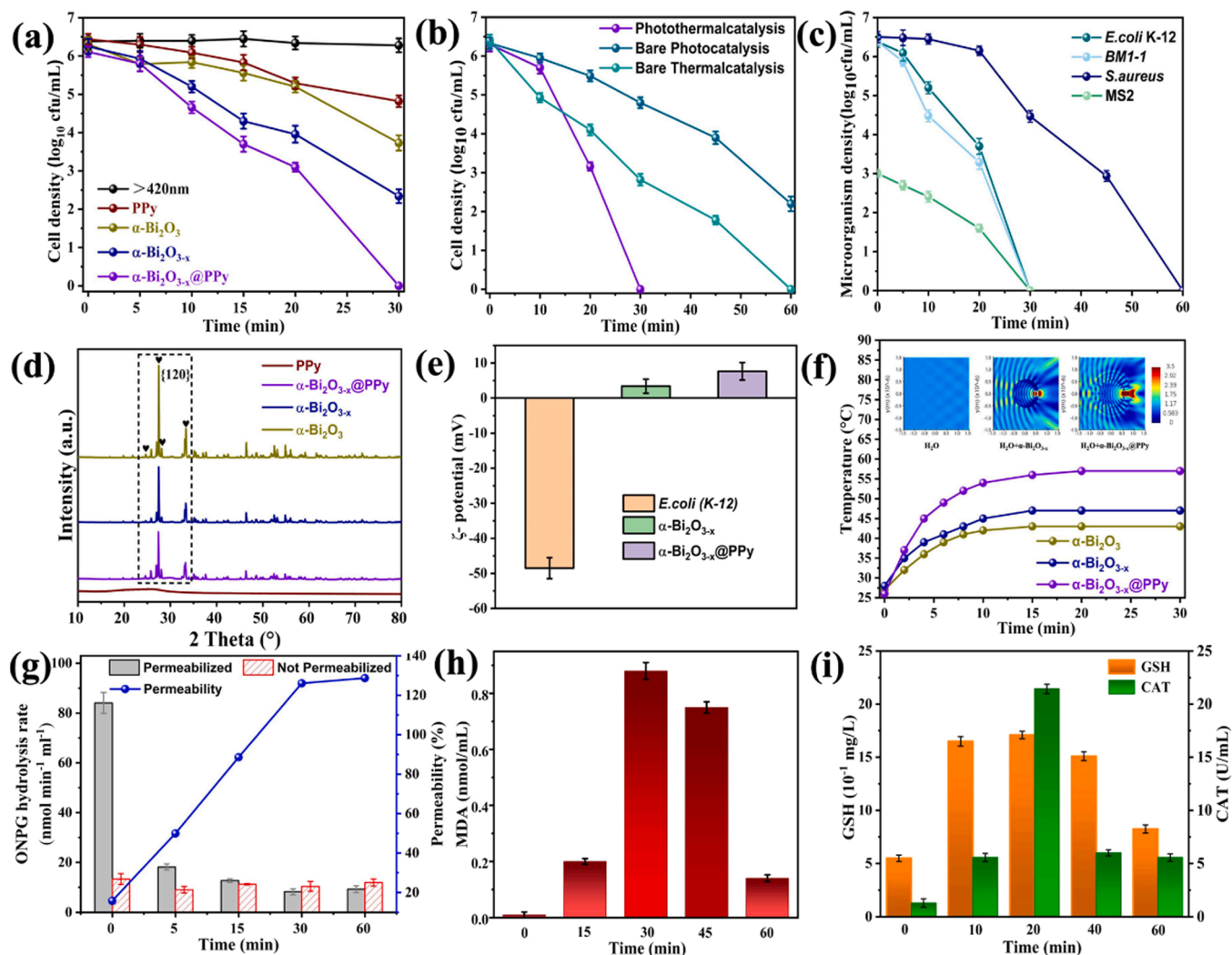
Fig. 1. (a) Inactivation efficiency of PPy, α-Bi$_2$O$_3$, α-Bi$_2$O$_{3-x}$, α-Bi$_2$O$_{3-x}$ @PPy under vis-NIR irradiation for *E. coli* K-12; (b) Inactivation efficiency of photothermal catalysis, bare photocatalytic system, and bare thermal system for *E. coli* K-12 (Bare photocatalytic system: only under vis-IR irradiation at the constant room temperature; bare thermal system: only at the simulated temperature of 57 ℃ without vis-IR irradiation); (c) Inactivation performance toward different pathogens by α-Bi$_2$O$_{3-x}$ @PPy under vis-NIR irradiation.; (d) XRD patterns of α-Bi$_2$O$_3$, α-Bi$_2$O$_{3-x}$ and α-Bi$_2$O$_{3-x}$ @PPy; (e) ζ-potentials of *E. coli* K-12, α-Bi$_2$O$_3$, and α-Bi$_2$O$_{3-x}$ @PPy at PH= 7; (f) Solution temperature under simulated sunlight irradiation and FDTD simulation of photoelectric field (inset) for the α-Bi$_2$O$_{3-x}$ and α-Bi$_2$O$_{3-x}$ @PPy. (g) The cell membrane permeability of the *E. coli* K-12 determined by ONPG hydrolysis assay; (h) The MDA yields with the contact time in the α-Bi$_2$O$_{3-x}$ @PPy/vis-NIR system; (i) The GSH and CAT yields with the contact time in the α-Bi$_2$O$_{3-x}$ @PPy/vis-NIR system.

contrast to the α-Bi$_2$O$_{3-x}$, which will be capable of physically assembling the strong negative-charged surface of *E. coli* K-12 cell membrane [36, 37]. This speculation is solidly confirmed by the SEM images of the bacterial assembly onto the α-Bi$_2$O$_{3-x}$ @PPy (Fig. S7). Beyond, the physical assembly of *E. coli* K-12 onto the bare PPy and α-Bi$_2$O$_{3-x}$ @PPy behaves the non-negligible sterilization performance compared with the bare α-Bi$_2$O$_{3-x}$ (Fig. S8). This assembly of the bacteria might significantly enhance the mass-transfer efficiency between bacterial cell-membrane and the α-Bi$_2$O$_{3-x}$ @PPy, further greatly benefiting the sterilization performance [38,39]. Besides, the α-Bi$_2$O$_{3-x}$ @PPy is capable of the superior photothermal ability over the bare α-Bi$_2$O$_{3-x}$ and PPy. The results (Fig. 1f) show that the bulk solution is heated up to 57 ℃ within 30 min by the α-Bi$_2$O$_{3-x}$ @PPy, much higher than 43 ℃ and 47 ℃ by the α-Bi$_2$O$_3$ and α-Bi$_2$O$_{3-x}$, respectively. And the simulated sunlight irradiation experiment (Fig. S9) states the local interfacial temperature of the α-Bi$_2$O$_{3-x}$ @PPy can reach up to 94.4 ℃ within 10 min, two times higher than that of both α-Bi$_2$O$_3$ and α-Bi$_2$O$_{3-x}$, confirming the superior photothermal ability of the α-Bi$_2$O$_{3-x}$ @PPy. The FDTD simulation (inset in Fig. 1f) shows that the α-Bi$_2$O$_{3-x}$ @PPy can generate a much stronger photoelectric field than others, which

reveals that the more efficient separation of photoelectrons and charges occurred and further enhanced the charge transfer and photothermal ability in the α-Bi$_2$O$_{3-x}$ @PPy/vis-NIR system [40,41].

As well-known, the high temperature can cause the thermal protein deformation on the *E. coli* K-12 cell membranes thus enhancing its permeability [42,43]. The permeability of the *E. coli* K-12 cell membranes in the α-Bi$_2$O$_{3-x}$ @PPy/vis-NIR system was determined by the ONPG hydrolysis assay. ONPG, as an indicator, can be hydrolyzed by the enzymes inside the *E. coli* K-12 cell causing the upgoing value of OD$_{420}$, which is strongly related to the increased permeability of the *E. coli* K-12 cell membranes [44]. The results in Fig. 1g clearly show that the permeability of the *E. coli* K-12 cell membranes rapidly reached up to 100% within 30 min, indicating that the inner membrane was gradually destroyed [45]. Besides, the results of malondialdehyde (MDA) yield (Fig. 1h), which is the most widely applied biomarker for lipid peroxidation on the cell membranes, show that the MDA yields significantly increased up to 0.88 nmol/mL within the first 30 min and sharply decreased to 0.14 nmol/mL at 60 min. This phenomenon directly confirms the lipid peroxidation on the cell membranes occurred and led to the permeability increase of cell membranes in this system [46].

Furthermore, the fluorescence microscopic images (Fig. S10) reveal that the green fluorescence of the assembled *E. coli* K-12 cells at initial stage (0 min) turned to red fluorescence after 30 min treatment in the α-Bi$_2$O$_{3-x}$@PPy/vis-NIR system. This phenomenon validates that the permeability of the *E. coli* K-12 cell membranes assembled on the α-Bi$_2$O$_{3-x}$@PPy was completely unbolted [47,48]. Thus, the above discussions demonstrated that the photothermal effects in the α-Bi$_2$O$_{3-x}$@PPy/vis-NIR system can cause the thermal damage of the *E. coli* K-12 cell membranes, conducive to the sterilization performance. Beyond this, the yields of GSH and CAT, the antioxidant enzymes as the indicators for the $\bullet$O$_2^-$, H$_2$O$_2$, and $\bullet$OH oxidation stresses towards the outer and inner bacterial cells, were evaluated [49]. From the results (Fig. 1i), we found the same trend that the yields gradually increased first and significantly decreased behind for both GSH and CAT. This phenomenon reveals that the bacterial cells experienced the violent oxidative assaults of ROS until its defense function was destroyed, further fatally losing the metabolic function [45,50]. To this end, the above discoveries clearly validate that the oxidative assaults greatly contribute to the fatal inactivation towards the bacteria beyond the contributions of physical adhesion and photothermal effects. Therefore, to better understand the mechanisms of sterilization performance, the insights into the fatal oxidative assaults need to be investigated.

3.3. Probing the mechanisms of the fatal oxidative assaults

To investigate the primary contributors of the fatal oxidative assaults in the α-Bi$_2$O$_{3-x}$@PPy/vis-NIR system, the ESR test were conducted to identify the primary ROS. The results show that the characteristic peaks corresponding to ^{1}O$_2$ (Fig. S11) were found in all the systems of α-Bi$_2$O$_3$, α-Bi$_2$O$_{3-x}$, and α-Bi$_2$O$_{3-x}$@PPy under vis-NIR irradiation, while the intensity of ^{1}O$_2$ shows complete no difference among these systems, which indicates that the ^{1}O$_2$ is not the oxidative assaulter for the sterilization performance. In contrast, the $\bullet$O$_2^-$ (Fig. 2a) and $\bullet$OH (Fig. 2b) were also detected in all systems but, noteworthily, the signal intensity of $\bullet$O$_2^-$ and $\bullet$OH in the α-Bi$_2$O$_{3-x}$@PPy/vis-NIR system is much stronger over that in α-Bi$_2$O$_3$/vis-NIR and α-Bi$_2$O$_{3-x}$/vis-NIR systems. This phenomenon demonstrates that the $\bullet$O$_2^-$ and $\bullet$OH could be the dominant oxidative assaulters to the great sterilization performance in the α-Bi$_2$O$_{3-x}$@PPy/vis-NIR system. Furthermore, the results of quenching study (Fig. 2c) confirmed the $\bullet$O$_2^-$, $\bullet$OH, and H$_2$O$_2$ are the oxidative assaulters contribute to the sterilization performance, following the order of $\bullet$O$_2^->$H$_2$O$_2 > \bullet$OH. As known broadly, the H$_2$O, $\bullet$O$_2^-$, and O$_2$

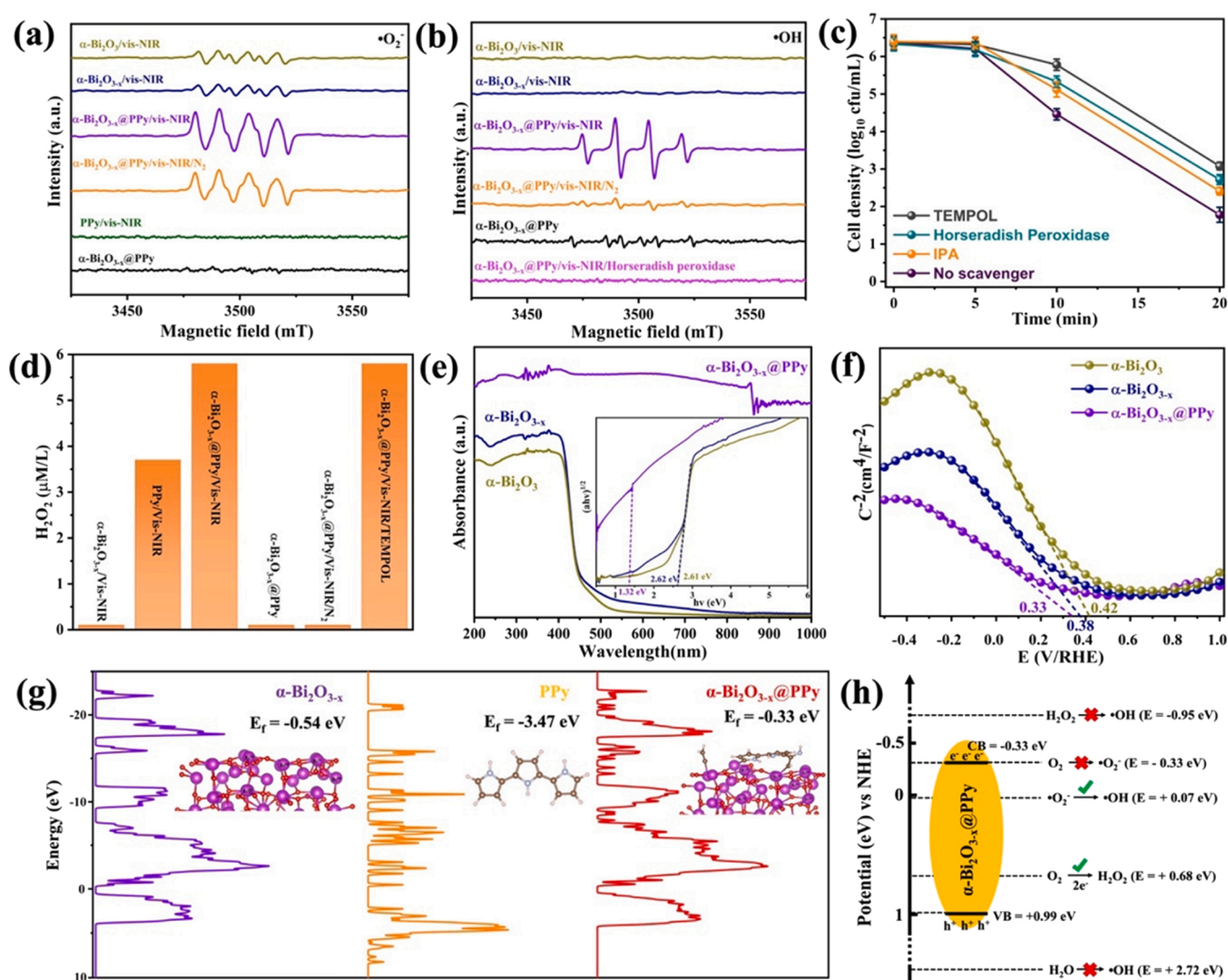**Fig. 2.** ESR spectra of $\bullet$O$_2^-$ (a) and $\bullet$OH (b) in various systems; (c) Quenching study of $\bullet$O$_2$, $\bullet$OH, and H$_2$O$_2$ (TEMPOL, Horseradish peroxidase, and IPA as the scavengers for $\bullet$O$_2^-$, H$_2$O$_2$, and $\bullet$OH, respectively) in the α-Bi$_2$O$_{3-x}$@PPy/vis-NIR system; (d) H$_2$O$_2$ generation at the moment of 30 min in various systems; (e) UV-Vis-NIR DRS spectra of the α-Bi$_2$O$_3$, α-Bi$_2$O$_{3-x}$, and α-Bi$_2$O$_{3-x}$@PPy and the corresponding the Tauc plots (inset); (f) Mott-Schottky plots of the α-Bi$_2$O$_3$, α-Bi$_2$O$_{3-x}$, and α-Bi$_2$O$_{3-x}$@PPy; (g) The TDOS spectra for α-Bi$_2$O$_{3-x}$, PPy, and α-Bi$_2$O$_{3-x}$@PPy; (h) Schematic diagram for the bandgap structure of the α-Bi$_2$O$_{3-x}$@PPy.

could be the key precursors for the H_2O_2 generation [51]. The H_2O_2 generated in the $\alpha\text{-}Bi_2O_{3-x}$ @PPy/vis-NIR system were successfully detected by the DPD-POD method [52]. The results in Fig. 2**d** declare that the $\alpha\text{-}Bi_2O_{3-x}$ @PPy/vis-NIR system behaved the prominent H_2O_2 yields over the other systems. By contrast, the systems of bare $\alpha\text{-}Bi_2O_{3-x}$ @PPy, $\alpha\text{-}Bi_2O_{3-x}$/vis-NIR, and $\alpha\text{-}Bi_2O_{3-x}$ @PPy/vis-NIR/N_2 behaved the complete no yield of H_2O_2, while the PPy/vis-NIR behaved the non-negligible H_2O_2 yield compared with the $\alpha\text{-}Bi_2O_{3-x}$ @PPy/vis-NIR system. These results indicate that the H_2O_2 generation was primarily attributed to the PPy component and the dissolved O_2, and the complexed $\alpha\text{-}Bi_2O_{3-x}$ component enhances the H_2O_2 yields in the $\alpha\text{-}Bi_2O_{3-x}$ @PPy/vis-NIR system [53]. Furthermore, the TEMPOL as the $\bullet O_2^-$ scavenger were added into the $\alpha\text{-}Bi_2O_{3-x}$ @PPy/vis-NIR system to probe the role of $\bullet O_2^-$ in the H_2O_2 generation. The result indicates that the $\bullet O_2^-$ did not contribute to the H_2O_2 generation in terms of the unchanged H_2O_2 yields with and without adding TEMPOL in the $\alpha\text{-}Bi_2O_{3-x}$ @PPy/vis-NIR system. Therefore, it can be deduced that the self-generated H_2O_2 derived from the dissolved O_2 reduction via the two-electron O_2 reduction pathway (ORR, Eq. (1), $E_{(O2/H2O2)}$ = +0.68 eV vs NHE) [54].

$$O_2 + 2e^- + H^+ \rightarrow H_2O_2 \qquad (1)$$

To this end, we have identified that the $\bullet O_2^-$ is the most primary oxidative assaulter and the self-generated H_2O_2 attributed to the PPy component and dissolved O_2 is also a nonnegligible oxidative assaulter for the great sterilization performance. While the $\bullet OH$ as the third oxidative assaulter could probably derive from the self-generated H_2O_2 activation, which will be comprehensively discussed below. So accordingly, we reasonably speculate that the $\alpha\text{-}Bi_2O_{3-x}$ component could function the selective generation of $\bullet O_2^-$ via two main possible pathways: (I) the photocatalytic O_2 reduction ($E(O_2/\bullet O_2^-)$ = −0.33 eV vs NHE) [55]; (II) the selective photocatalytic activation of the interfacial structural oxygen (O_{lat}/O_{ads}) that contains lattice oxygen (O_{lat}) and adsorbed oxygen (O_{ads}). Besides, for the $\bullet OH$ generation, it could usually be achieved by the following possible pathways: (I) the photocatalytic self-activation of H_2O_2 ($E(H_2O_2/\bullet OH)$ = −0.95 eV vs NHE) [53,56]. (II) the photocatalytic H_2O oxidation ($E(H_2O/\bullet OH)$ = +2.72 eV vs NHE) [55,57]. (III) the photocatalytic $\bullet O_2^-$ conversions ($E(\bullet O_2^-/\bullet OH)$ = +0.07 eV vs NHE) [54,55]. (IV) the photocatalytic activation of self-generated H_2O_2 on the high-coordinated Bi^V/Bi^{IV}. Therefore, to understand how the $\bullet O_2^-$ is selectively generated and what is the exact $\bullet OH$ generation pathway is imperative for the mechanisms of sterilization performance in the $\alpha\text{-}Bi_2O_{3-x}$ @PPy/vis-NIR system.

Explicitly, the UV-Vis-NIR diffuse reflectance spectra (DRS) tests were conducted to determine the adsorption edge of the catalysts, and the bandgaps were calculated by Kubelka-Munk formula [58]. According to Fig. 2**e**, the corresponding bandgaps for $\alpha\text{-}Bi_2O_3$, $\alpha\text{-}Bi_2O_{3-x}$, and $\alpha\text{-}Bi_2O_{3-x}$ @PPy are calculated to be 2.61 eV, 2.62 eV, and 1.32 eV using the Tauc plot method, respectively [35,59]. These phenomena mean that the $\alpha\text{-}Bi_2O_{3-x}$ @PPy is capable of adsorbing lights in the near-infrared range, which distinguishes $\alpha\text{-}Bi_2O_{3-x}$ @PPy from the $\alpha\text{-}Bi_2O_3$ and $\alpha\text{-}Bi_2O_{3-x}$, owing to the complexed PPy component. Hence, the $\alpha\text{-}Bi_2O_{3-x}$ @PPy should consequently behave a great photothermal ability in theories, which has been validated by the experimental results as discussed above. Furthermore, the Mott-Schottky test was employed to probe the band position of the catalysts. In Fig. 2**f**, the conduct band (CB) position of the $\alpha\text{-}Bi_2O_{3-x}$ @PPy is found to be − 0.33 eV, and consequently, the corresponding valence band (VB) position is calculated to be 0.99 eV. Additionally, the TDOS spectra and Fermi energy (E_f) for $\alpha\text{-}Bi_2O_{3-x}$, PPy, and $\alpha\text{-}Bi_2O_{3-x}$ @PPy were calculated as shown in Fig. 2**g**. The $\alpha\text{-}Bi_2O_{3-x}$ shows a much more positive E_f of − 0.54 eV than the PPy with the E_f of − 3.47 eV, indicating that the electrons intend to migrate from the $\alpha\text{-}Bi_2O_{3-x}$ component to the PPy component in the $\alpha\text{-}Bi_2O_{3-x}$ @PPy [60]. This phenomenon points out that the complexed PPy promote creating the high-coordinated Bi^V/Bi^{IV} sites in the $\alpha\text{-}Bi_2O_{3-x}$ @PPy. Besides, the $\alpha\text{-}Bi_2O_{3-x}$ @PPy possesses a E_f of

− 0.33 eV, which is higher than both $\alpha\text{-}Bi_2O_{3-x}$ and PPy revealing that the $\alpha\text{-}Bi_2O_{3-x}$ @PPy has a lower energy barrier to excite the photo-catalytical separation of electrons and charges [12].

Thus, to sum up in Fig. 2**h**, it can be clarified that the pathway I and II for the $\bullet OH$ generation is not feasible via the photo-excited electron and charge because the $E(H_2O_2/\bullet OH)$ = −0.95 eV and $E(H_2O/\bullet OH)$ = +2.72 eV are much more negative and positive over CB and VB, respectively [61]. Besides, the experimental results in Fig. 2**a-b** have showed that the $\alpha\text{-}Bi_2O_{3-x}$ @PPy/vis-NIR/N_2 system without dissolved O_2 behaves a bit slight decrease in the $\bullet O_2^-$ signal intensity and shows the negligible $\bullet OH$ yields compared to the $\alpha\text{-}Bi_2O_{3-x}$ @PPy/vis-NIR system. This phenomenon experimentally confirms that the dissolved O_2 was selectively contributed to the H_2O_2 generation via two-electrons ORR beyond the $\bullet O_2^-$ generation. The negligible $\bullet O_2^-$ signal in the system of bare $\alpha\text{-}Bi_2O_{3-x}$ @PPy and PPy/vis-NIR (Fig. 2**a**) manifests that the $\bullet O_2^-$ generation is a photocatalytic process on the $\alpha\text{-}Bi_2O_{3-x}$ component. According to the $\bullet O_2^-$ signal intensity, it can be calculated that the $\bullet O_2^-$ generation is accomplished by the $\alpha\text{-}Bi_2O_{3-x}$ component with 80% selectivity, which matches the generation pathway II of the selective photocatalytic activation of interfacial (O_{lat}/O_{ads}).

Additionally, the weak characteristic peaks assigned to the carbon-centered radicals trapped by DMPO was observed in the bare $\alpha\text{-}Bi_2O_{3-x}$ @PPy system (Fig. 2**b**). This phenomenon indicates that complexing $\alpha\text{-}Bi_2O_{3-x}$ with PPy not only forms abundant high-coordinated Bi^V/Bi^{IV} sites but also produces a few carbon-centered radicals from the PPy component. The similar observation can be found and supported by the literature [62,63]. However, the characteristic peaks of the carbon-centered radicals disappeared once the light was introduced, which is probably owing to that the DMPO prefers to react with the $\bullet OH$ beyond the carbon-centered radicals. To this end, the complete no $\bullet OH$ signal in the $\alpha\text{-}Bi_2O_{3-x}$ @PPy/vis-NIR/Horseradish peroxidase system and the bare $\alpha\text{-}Bi_2O_{3-x}$ @PPy system claim that the $\bullet OH$ generation is completely caused by the photocatalytic activation of self-generated H_2O_2. Moreover, according to Fig. 2**h**, the dissolved O_2 in the system would be selectively reduced to H_2O_2 rather than $\bullet O_2^-$ by the photo-excited electrons on the $\alpha\text{-}Bi_2O_{3-x}$ @PPy because the $E(O_2/H_2O_2)$ = +0.68 eV has a much less energy barrier to break through than the $E(O_2/\bullet O_2^-)$ = −0.33 eV. Therefore, the above results solidly validated that the $\bullet O_2^-$ was primarily generated by the activation of interfacial (O_{lat}/O_{ads}) (pathway II) with the 80% selectivity in the system. Additionally, it also validates that the $\bullet OH$ was most likely generated by the photocatalytic activation of self-generated H_2O_2 on the high-coordinated Bi^V/Bi^{IV} (pathway IV) rather than the $\bullet O_2^-$ conversion (pathway III). At this point, the generation pathways of $\bullet O_2^-$, H_2O_2, and $\bullet OH$ has been clarified to be the selective photocatalytic activation of interfacial (O_{lat}/O_{ads}) (pathway II), the two-electron ORR process, and the photocatalytic activation of self-generated H_2O_2 on the high-coordinated Bi^V/Bi^{IV} (pathway IV), respectively. However, the deeper insights into the mechanisms that what is exact reaction to generate the $\bullet O_2^-$, H_2O_2, and $\bullet OH$ in the $\alpha\text{-}Bi_2O_{3-x}$ @PPy/vis-NIR system are still unclear.

To probe the deeper mechanisms, the XPS, in situ Raman, and DFT calculations were conducted. The XPS wide spectra of $\alpha\text{-}Bi_2O_{3-x}$, $\alpha\text{-}Bi_2O_{3-x}$ @PPy, and spent $\alpha\text{-}Bi_2O_{3-x}$ @PPy in Fig. S12 demonstrate the presence of expected compositions among these samples, confirming that the $\alpha\text{-}Bi_2O_{3-x}$ and PPy were successfully complexed. Furthermore, the Bi 4 f spectra of all samples (Fig. 3**a**) commonly present the characteristic peaks at 159.01 eV and 164.41 eV assigning to the Bi 4 $f_{7/2}$ and Bi 4 $f_{5/2}$, respectively [8,30,59,61]. Intriguingly, the characteristic peak of Bi 4 f show a significant red shift of 0.76 eV in binding energy after complexing with PPy revealing a electrons-donated process occurred upon Bi. This result indicates that the complexed PPy could function grabbing electrons from the relative low-coordinated Bi^{III}, consequently transforming Bi^{III} to the high-coordinated Bi^V/Bi^{IV} [64]. Theoretically, the DFT calculation directly proves the alterations from the low-coordinated Bi^{III} to the higher-coordinated Bi^V/Bi^{IV} that the outer electrons of Bi^{III} was grabbed by the C-N skeleton as the electrons
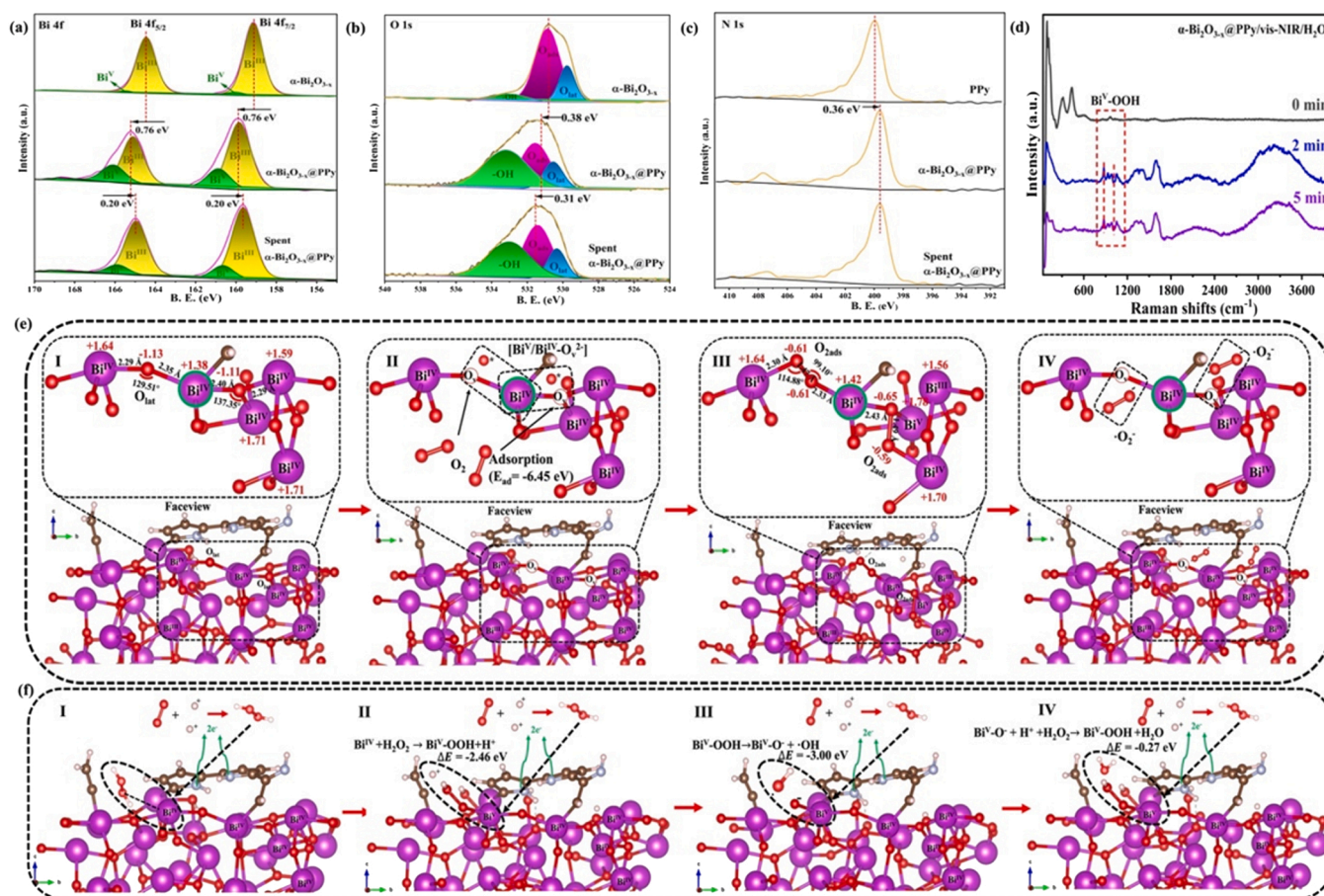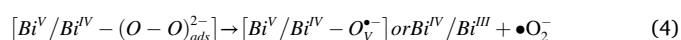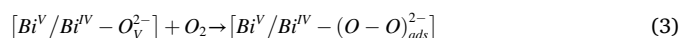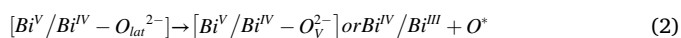
Fig. 3. XPS spectra of the samples of (a) Bi 4 f; (b) O 1 s; and (c) N 1 s (All the spectra were calibrated by C 1 s); (d) in situ Raman spectra in the α-Bi$_2$O$_{3-x}$ @PPy/Vis-NIR/H$_2$O$_2$ system; The high-coordinated Bi^{IV}/Bi^V regulates the selective generation of •O$_2^-$ (e) and activation of self-generated H$_2$O$_2$ (f) in terms of DFT calculations.

acceptor in terms of Bader charge results. The green circled Bi^{III} with the charge state of donating 1.14 electrons (+1.14 e) in the modeled α-Bi$_2$O$_{3-x}$ (Fig. S13) donated more electrons up to + 1.38 e with transforming to the higher-coordinated Bi^V/Bi^{IV} after complexing with the PPy in the modeled α-Bi$_2$O$_{3-x}$ @PPy (Fig. 3e(I)). Indeed, the corresponding C in the PPy component bonded with the Bi^{III} grabbed more electrons causing the charge state increased from − 0.11 (Fig. S14) to − 0.62 e (Fig. S15). These results solidly confirm that the complexed PPy component functions transforming the low-coordinated Bi^{III} to the higher-coordinated Bi^V/Bi^{IV} by reconstructing the local charge landscape. Besides, according to the O 1 s spectra in Fig. 3**b**, the common main characteristic peak at 530.81 eV also shows an apparent red shift of 0.38 eV in binding energy from the α-Bi$_2$O$_{3-x}$ to the α-Bi$_2$O$_{3-x}$ @PPy indicating the similar electrons-donated process occurred on the O$_{lat}$/O$_{ads}$. Notably, the occurrence of the electrons-donated process on the O$_{lat}$/O$_{ads}$ is accomplished by the diffusions of O$_{lat}$/O$_{ads}$ in the surface of catalysts, which is well-known by the reported works [65,66]. Not only that, the O$_{lat}$/O$_{ads}$ diffusion efficiency shows a strong positive relation to the quantity of oxygen vacancies (O$_v$) and greatly benefits the O$_{lat}$/O$_{ads}$ activation. Thus, the EPR result (Fig. S16) reports that the α-Bi$_2$O$_{3-x}$ @PPy possesses a much higher quantity of O$_v$ over the original α-Bi$_2$O$_{3-x}$ and α-Bi$_2$O$_3$, revealing it is capable of the much more efficient O$_{lat}$/O$_{ads}$ diffusions on its surface. Additionally, the N 1 s spectra (Fig. 3**c**) shows a significant blue shift of 0.36 eV in binding energy from the PPy to the α-Bi$_2$O$_{3-x}$ @PPy indicating that the N atoms in the C-N skeleton of PPy could be the active sites that assembled the grabbed electrons from the low-coordinated Bi^{III} [13]. Hence, it can be reasonably speculated that the complexing of PPy accomplished grabbing electrons from the low-coordinated Bi^{III} to the N sites via Bi-C-N,
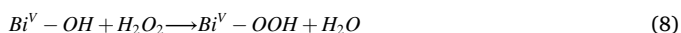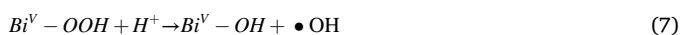
consequently creating the high-coordinated Bi^V/Bi^{IV} and inspiring the O$_{lat}$/O$_{ads}$ in the α-Bi$_2$O$_{3-x}$ @PPy. The similar phenomenon has been acknowledged as electron delocalization and reported in the literatures [21,27,28].

Intriguingly, a slight blue shift of 0.2 eV in binding energy for Bi^V/Bi^{IV} and an extra red shift of 0.31 eV in binding energy for O$_{lat}$/O$_{ads}$ are observed in the spent α-Bi$_2$O$_{3-x}$ @PPy compared to that in the α-Bi$_2$O$_{3-x}$ @PPy. This phenomenon discloses the fact that the selective •O$_2^-$ generation is simultaneously accompanied by the O$_{lat}$/O$_{ads}$ diffusions and the partial alterations from the high-coordinated Bi^V/Bi^{IV} to the low-coordinated Bi^{III}. To this end, it can be reasonably proposed that the selective •O$_2^-$ generation is accomplished by the O$_{lat}$/O$_{ads}$ activation triggered by the high-coordinated Bi^V/Bi^{IV} sites on the surface of α-Bi$_2$O$_{3-x}$ @PPy. Explicitly, the O$_{lat}$ bonding to high-coordinated Bi^V/Bi^{IV} atoms will be photo-catalytically activated and released with the O$_v$ left behind under the vis-NIR irradiation, consequently forming the [Bi^V/Bi^{IV}-O$_v^{2-}$] sites as the Eq. (2) [64,66]. Then, the created O$_v$ will be easily occupied by the O$_2$ molecules forming the $\left[Bi^V/Bi^{IV} - (O-O)_{ads}^{2-} \right]$ sites as the Eq. (3). Consequently, the outer electrons from the high-coordinated Bi^V/Bi^{IV} will be photo-catalytically excited to activate the adjacent (O-O)$_{ads}$ further selectively produce the •O$_2^-$ as the Eq. (4). In the aspect of DFT calculation, the two adjacent O$_{lat}$ bonding to the high-coordinated Bi^{IV} atom (green circle) show the charge state of − 1.13 e and - 1.11 e with the bond length of 2.35 Å and 2.40 Å, respectively, at the initial stage (Fig. 3e(I)). Thus, the unbalanced charge state impels the two O$_{lat}$ to be easily activated by the photo-excited electrons from the bonded Bi^{IV} atom, consequently leaving the O$_v$ behind. Therewith, the two free O$_2$ molecules will be spontaneously adsorbed on the two O$_v$ with the total adsorption energy of − 6.45 eV

(Fig. 3e(II)). Accordingly, the adsorbed O_2 are inspired into an active state in terms of the higher charge state of -1.22 e and -1.24 e in total indicating that the adsorbed O_2 gained more electrons from the surrounding atoms (Fig. 3e(III)) compared to the initial charge state of O_{lat}. This phenomenon can also be confirmed by the visualization of the charge density difference in the two states (Fig. S17). Correspondingly, the bonded high-coordinated Bi^{IV}/Bi^V atoms show an overall decrease in the charge state after the O_2 adsorption, which is consistent with the foregoing discussions (Fig. 3e(III)). Then, the active adsorbed O_2 will be easily triggered to selectively generate $\bullet O_2^-$ under the vis-NIR irradiation (Fig. 3e(IV)). These DFT calculations theoretically validates the process of the selective generation of $\bullet O_2^-$ modulated by the high-coordinated Bi^{IV}/Bi^V in the photo-catalytical system.

$$[Bi^V/Bi^{IV} - O_{lat}{}^{2-}] \rightarrow [Bi^V/Bi^{IV} - O_V^{2-}] \, or \, Bi^{IV}/Bi^{III} + O^* \quad (2)$$

$$[Bi^V/Bi^{IV} - O_V^{2-}] + O_2 \rightarrow [Bi^V/Bi^{IV} - (O-O)_{ads}^{2-}] \quad (3)$$

$$[Bi^V/Bi^{IV} - (O-O)_{ads}^{2-}] \rightarrow [Bi^V/Bi^{IV} - O_V^{\bullet-}] \, or \, Bi^{IV}/Bi^{III} + \bullet O_2^- \quad (4)$$

Besides, the self-generated H_2O_2 as the secondary oxidative assaulter is non-negligible for the sterilization performance in this system. The H_2O_2 self-generation has been confirmed to be achieved via ORR on the PPy component. As discussed above, the PPy component as the electrons acceptor that function creating Bi^V/Bi^{IV} by grabbing electrons from Bi^{III} are apparently the reactive sites for the H_2O_2 self-generation, which is acknowledged by the reported studies [52,67,68]. As we discovered above, the self-generated H_2O_2 as the secondary oxidative assaulter will mostly be activated to produce $\bullet OH$ by the H_2O_2 activation on the high-coordinated Bi^V/Bi^{IV} (pathway IV) in the system. For this case, we proposed that the high-coordinated Bi^{IV}/Bi^V regulates the photo-catalytical activation of the self-generated H_2O_2 to produce $\bullet OH$ as the Eqs. (5)–(8). Initially, the high-coordinated Bi^{IV} will react with H_2O_2 to generate a reactive mediator of Bi^V-OOH as the Eqs. (5)–(6) with the change of relative energy (ΔE) = -2.46 eV (Fig. 3f(I-II)). Besides, the charge state of the Bi^V in the Bi^V-OOH is $+1.70$ e (Fig. S18) higher than the $+1.64$ e before the formation of Bi^V-OOH, confirming that the Bi^{IV} donated more electrons to form the active Bi^V-OOH mediator. Moreover, the visualization of the charge density distribution (Fig. S19) also confirms that the more electrons were grabbed from the Bi^{IV} to the O atoms in the Bi^V-OOH. Then, the Bi^V/Bi^{IV}-OOH will further willingly decompound to the mediator of Bi^V/Bi^{IV}-OH with the production of $\bullet OH$ as the Eq. (7) with the $\Delta E = -3.00$ eV (Fig. 3f(III)) [22]. Finally, the Bi^V/Bi^{IV}-OH will react with H_2O_2 to generate the Bi^V/Bi^{IV}-OOH again as the Eq. (8) with the $\Delta E = -0.27$ eV, which forms alternative reaction circle to consecutively produce $\bullet OH$ by activating H_2O_2 (Fig. 3f(IV)). To experimentally validate this speculation, the in situ Raman tests for the α-Bi_2O_{3-x} @PPy/Vis-NIR with the additional H_2O_2 treatment were conducted. The results manifest that the new peaks at 850–1050 cm^{-1} assigned to the characteritic signal of Bi^V/Bi^{IV}-OOH show up apparently at the moment of 2 and 5 min after H_2O_2 treatment in contrast to that at 0 min. This phenomenon directly confirms that the mediator of Bi^V/Bi^{IV}-OOH formed during the H_2O_2 activation process, which has been simaially reported by other study [8,22].

$$H_2O_2 \rightarrow HOO^- + H^+ \quad (5)$$

$$Bi^{IV} + HOO^- \rightarrow Bi^V - OOH \quad (6)$$

$$Bi^V - OOH + H^+ \rightarrow Bi^V - OH + \bullet OH \quad (7)$$

$$Bi^V - OH + H_2O_2 \longrightarrow Bi^V - OOH + H_2O \quad (8)$$

4. Conclusions

This study proposed an advanced sterilization strategy that the high-coordinated Bi^V/Bi^{IV} regulates the selective activation of structural

oxygen (O_{lat}/O_{ads}) and self-generated H_2O_2 as the fatal assault assisted by the multi-physical-like effects for the efficient sterilization performance, which could enrich the knowledge of selective oxidation applications in sterilization strategy. The mutual physical adhesion and photothermal effects functions the physical-like damage for the cell membranes, which greatly benefits the further fatal oxidative assaults from the selective-generated $\bullet O_2^-$ and self-generated H_2O_2 and its activation towards the bacteria. Explicitly, this study comprehensively clarified the synergistic sterilization mechanisms including: (I) the physical adhesion towards the bacteria via electrostatic attraction will significantly enhance the mass transfer efficiency between the α-Bi_2O_{3-x} @PPy and bacteria and the photothermal effects prominently increase the permeability of cell membrane, which greatly promotes the fatal oxidative assaulters entering the bacteria interior. (II) the H_2O_2 was generated on the skeleton C-N sites of PPy component via the photocatalytic two-electrons ORR process and further activated on the high-coordinated Bi^{IV}/Bi^V to produce $\bullet OH$. (III) the Bi^V/Bi^{IV} regulates the $\bullet O_2^-$ generation with around 80% selectivity by activating the adjacent O_{lat}/O_{ads}, contributing the primary fatal oxidative assault towards the sterilization performance. Conclusively, this study not only enriches the fundamental principles for selective oxidation theories but also provides an advanced sterilization strategy for the practice applications.

CRediT authorship Contribution Statement

Qiyu Lian: Conceptualization, Investigation, Writing – original draft. **Zhuocheng Liang**: Investigation, Writing – original draft. **Xinyi Guan**: Visualization. **Zhuoyun Tang**: Investigation. **Rumeng Zhang**: Methodology. **Boyi Yang**: Methodology. **Yingxin Wu**: Methodology. **Huinan Zhao**: Methodology. **Chun He**: Supervision, Funding acquisition. **Dehua Xia**: Writing – review & editing, Supervision, Funding acquisition.

Declaration of Competing Interest

The authors declare that they have no known competing financial interests or personal relationships that could have appeared to influence the work reported in this paper.

Data Availability

Data will be made available on request.

Acknowledgements

Supporting Information

Supporting information is supplied for supported description and results.

Appendix A. Supporting information

Supplementary data associated with this article can be found in the online version at doi:10.1016/j.apcatb.2023.122724.

References

[1] M. Tavakolian, S.M. Jafari, T.G.M. van de Ven, A review on surface-functionalized cellulosic nanostructures as biocompatible antibacterial, Mater., Nano-Micro Lett. 12 (2020) 73.

[2] T. Wang, Z. Jiang, T. An, G. Li, H. Zhao, P.K. Wong, Enhanced visible-light-driven photocatalytic bacterial inactivation by ultrathin carbon-coated magnetic cobalt ferrite nanoparticles, Environ. Sci. Technol. 52 (2018) 4774–4784.

[3] W. Wang, H. Xie, G. Li, J. Li, P.K. Wong, T. An, Visible light-induced marine bacterial inactivation in seawater by an in situ photo-fenton system without additional oxidants: implications for ballast water sterilization, ACS ES&T, Water 1 (2021) 1483–1494.

[4] P. Zhang, Z. Guo, C. Chen, I. Lynch, Uncertainties in the antibacterial mechanisms of graphene family materials, Nano Today 43 (2022), 101436.

[5] X. Kong, X. Liu, Y. Zheng, P.K. Chu, Y. Zhang, S. Wu, Graphitic carbon nitride-based materials for photocatalytic antibacterial application, Mater. Sci. Eng. R. 145 (2021), 100610.

[6] H. Zheng, Z. Ji, K.R. Roy, M. Gao, Y. Pan, X. Cai, L. Wang, W. Li, C.H. Chang, C. Kaweeteerawat, C. Chen, T. Xia, Y. Zhao, R. Li, Engineered graphene oxide nanocomposite capable of preventing the evolution of antimicrobial resistance, ACS Nano 13 (2019) 11488–11499.

[7] R. Li, N.D. Mansukhani, L.M. Guiney, Z. Ji, Y. Zhao, C.H. Chang, C.T. French, J. F. Miller, M.C. Hersam, A.E. Nel, T. Xia, Identification and optimization of carbon radicals on hydrated graphene oxide for ubiquitous antibacterial coatings, ACS Nano 10 (2016) 10966–10980.

[8] M. Yang, S. Qiu, E. Coy, S. Li, K. Załęski, Y. Zhang, H. Pan, G. Wang, NIR-responsive TiO₂ biometasurfaces: toward in situ photodynamic antibacterial therapy for biomedical implants, Adv. Mater. 34 (2021) 2106314.

[9] L. Wang, X. Zhang, X. Yu, F. Gao, Z. Shen, X. Zhang, S. Ge, J. Liu, Z. Gu, C. Chen, An all-organic semiconductor C₃N₄/PDINH heterostructure with advanced antibacterial photocatalytic therapy activity, Adv. Mater. 31 (2019) 1901965.

[10] X. Zou, L. Zhang, Z. Wang, Y. Luo, Mechanisms of the antimicrobial activities of graphene materials, J. Am. Chem. Soc. 138 (2016) 2064–2077.

[11] A.C. Barrios, Y. Wang, L.M. Gilbertson, F. Perreault, Structure-property-toxicity relationships of graphene oxide: role of surface chemistry on the mechanisms of interaction with bacteria, Environ. Sci. Technol. 53 (2019) 14679–14687.

[12] X. Yue, L. Cheng, J. Fan, Q. Xiang, 2D/2D BiVO₄/CsPbBr₃ S-scheme heterojunction for photocatalytic CO₂ reduction: Insights into structure regulation and Fermi level modulation, Appl. Catal. B: Environ. 304 (2022), 120979.

[13] X. Zhou, Q. Shen, K. Yuan, W. Yang, Q. Chen, Z. Geng, J. Zhang, X. Shao, W. Chen, G. Xu, X. Yang, K. Wu, Unraveling charge state of supported Au single-atoms during CO oxidation, J. Am. Chem. Soc. 140 (2018) 554–557.

[14] Y. Zhang, X. Zhi, J.R. Harmer, H. Xu, K. Davey, J. Ran, S.Z. Qiao, Facet-specific active surface regulation of BiₓMOᵧ (M=Mo, V, W) nanosheets for boosted photocatalytic CO₂ reduction, Angew. Chem. Int. Ed. 61 (2022) e202212355.

[15] L.S. Zhang, X.H. Jiang, Z.A. Zhong, L. Tian, Q. Sun, Y.T. Cui, X. Lu, J.P. Zou, S. L. Luo, Carbon nitride supported high-loading Fe single-atom catalyst for activation of peroxymonosulfate to generate ¹O2 with 100% selectivity, Angew. Chem. Int. Ed. 60 (2021) 21751–21755.

[16] R. Zhang, C. Song, M. Kou, P. Yin, X. Jin, L. Wang, Y. Deng, B. Wang, D. Xia, P. K. Wong, L. Ye, Sterilization of Escherichia coli by photothermal synergy of WO₃₋ₓ/C nanosheet under infrared light irradiation, Environ. Sci. Technol. 54 (2020) 3691–3701.

[17] B.M. Mackey, C.A. Miles, D.A. Seymour, S.E. Parsons, Thermal denaturation and loss of viability in Escherichia coli and Bacillus stearothermophilus, Lett. Appl. Microbiol. 16 (1993) 56–58.

[18] Z. Qin, J.C. Bischof, Thermophysical and biological responses of gold nanoparticle laser heating, Chem. Soc. Rev. 41 (2012) 1191–1217.

[19] D. Xia, Q. Chen, Y. Jiao, Q. Lian, M. Sun, C. He, J. Shang, T. Wang, A modified flower pollen-based photothermocatalytic process for enhanced solar water disinfection: Photoelectric effect and bactericidal mechanisms, Water Res. 217 (2022), 118423.

[20] Z. Yang, J. Qian, C. Shan, H. Li, Y. Yin, B. Pan, Toward selective oxidation of contaminants in aqueous systems, Environ. Sci. Technol. 55 (2021) 14494–14514.

[21] Y. Gao, T. Wu, C. Yang, C. Ma, Z. Zhao, Z. Wu, S. Cao, W. Geng, Y. Wang, Y. Yao, Y. Zhang, C. Cheng, Activity trends and mechanisms in peroxymonosulfate-assisted catalytic production of singlet oxygen over atomic metal-N-C, Catal., Angew. Chem. Int. Ed. 60 (2021) 22513–22521.

[22] J. Wang, K.P. Hou, Y. Wen, H. Liu, H. Wang, K. Chakarawet, M. Gong, X. Yang, Interlayer structure manipulation of iron oxychloride by potassium cation intercalation to steer H₂O₂ activation pathway, J. Am. Chem. Soc. 144 (2022) 4294–4299.

[23] M.Y. Gao, H. Bai, X. Cui, S. Liu, S. Ling, T. Kong, B. Bai, C. Hu, Y. Dai, Y. Zhao, L. Zhang, J. Zhang, X. Xiong, Precisely tailoring heterometallic polyoxotitanium clusters for the efficient and selective photocatalytic oxidation of hydrocarbons, Angew. Chem. Int. Ed. 61 (2022), e202215540.

[24] L.D. Geoffrion, D. Medina-Cruz, M. Kusper, S. Elsaidi, F. Watanabe, P. Parajuli, A. Ponce, T.B. Hoang, T.J. Webster, G. Guisbiers, Bi₂O₃ nano-flakes as a cost-effective antibacterial agent, Nanoscale Adv. 3 (2021) 4106–4118.

[25] Y. Qiu, L. Zhang, L. Liu, C. Lin, L. Xu, J. Li, Y. Yuan, X. Du, Y. Han, J. Sun, Photoinduced synthesis of Bi₂O₃ nanotubes based on oriented attachment, J. Mater. Chem. A 7 (2019) 1424–1428.

[26] S. Loeb, C. Li, J.H. Kim, Solar photothermal disinfection using broadband-light absorbing gold nanoparticles and carbon black, Environ. Sci. Technol. 52 (2018) 205–213.

[27] H. Li, K. Gan, R. Li, H. Huang, J. Niu, Z. Chen, J. Zhou, Y. Yu, J. Qiu, X. He, Highly dispersed NiO clusters induced electron delocalization of Ni-N-C catalysts for enhanced CO₂ electroreduction, Adv. Funct. Mater. 33 (2022) 2208622.

[28] Z. Huang, J.-X. Liang, D. Tang, Y. Chen, W. Qu, X. Hu, J. Chen, Y. Dong, D. Xu, D. Golberg, J. Li, X. Tang, Interplay between remote single-atom active sites triggers speedy catalytic oxidation, Chem 8 (2022) 3008–3017.

[29] L. Midya, A. Chettri, S. Pal, Development of a novel nanocomposite using polypyrrole grafted chitosan-decorated CDs with improved photocatalytic activity under solar light illumination, ACS Sustain. Chem. Eng. 7 (2019) 9416–9421.

[30] W. Zhou, L. Lu, D. Chen, Z. Wang, J. Zhai, R. Wang, G. Tan, J. Mao, P. Yu, C. Ning, Construction of high surface potential polypyrrole nanorods with enhanced antibacterial properties, J. Mater. Chem. B 6 (2018) 3128–3135.

[31] B. Lei, W. Cui, J. Sheng, H. Wang, P. Chen, J. Li, Y. Sun, F. Dong, Synergistic effects of crystal structure and oxygen vacancy on Bi₂O₃ polymorphs: intermediates activation, photocatalytic reaction efficiency, and conversion pathway, Sci. Bull. 65 (2020) 467–476.

[32] S. Abdi, D. Dorranian, Effect of CTAB concentration on the properties of ZnO nanoparticles produced by laser ablation method in CTAB solution, Opt. Laser Technol. 108 (2018) 372–377.

[33] H. Chen, H. Yu, S. Cui, C. Liu, Effect oreferf PVP on gas-sensing properties of ZnO micro/nanostructure materials in SDS-PVP composite, Int. J. Appl. Ceram. Technol. 17 (2019) 1460–1466.

[34] S. Kumar, R.B. Choudhary, Influence of MnO₂ nanoparticles on the optical properties of polypyrrole matrix, Mater. Sci. Semicond. Process. 139 (2022), 106322.

[35] Q. Hao, Y. Liu, T. Chen, Q. Guo, W. Wei, B.-J. Ni, Bi₂O₃@Carbon nanocomposites for solar-driven photocatalytic degradation of chlorophenols, ACS Appl. Nano Mater. 2 (2019) 2308–2316.

[36] Q. Xia, X. Wang, Q. Zeng, D. Guo, Z. Zhu, H. Chen, H. Dong, Mechanisms of enhanced antibacterial activity by reduced chitosan-intercalated nontronite, Environ. Sci. Technol. 54 (2020) 5207–5217.

[37] A.P. Richter, J.S. Brown, B. Bharti, A. Wang, S. Gangwal, K. Houck, E.A. Cohen Hubal, V.N. Paunov, S.D. Stoyanov, O.D. Velev, An environmentally benign antimicrobial nanoparticle based on a silver-infused lignin core, Nat. Nanotechnol. 10 (2015) 817–823.

[38] R. Yang, B. Liang, S. Zheng, C. Hu, Y. Xu, Y. Ma, Y. Bai, K. Dai, Y. Tang, C. Zhang, M. Chang, Improving the surface oxygen vacancy concentration of Bi₂O₄ through the pretreatment of the NaBiO₃·2H₂O precursor as a high-performance visible light photocatalyst, Inorg. Chem. 61 (2022) 14102–14114.

[39] X. Li, H. Bai, Y. Wang, J. Yoon, S. Wang, X. Zhang, Supramolecular antibacterial materials for combatting antibiotic resistance, Adv. Mater. 31 (2019), e1805092.

[40] G. Yu, J. Qian, P. Zhang, B. Zhang, W. Zhang, W. Yan, G. Liu, Collective excitation of plasmon-coupled Au-nanochain boosts photocatalytic hydrogen evolution of semiconductor, Nat. Commun. 10 (2019) 4912.

[41] X. Li, H. Jiang, C. Ma, Z. Zhu, X. Song, H. Wang, P. Huo, X. Li, Local surface plasma resonance effect enhanced Z-scheme ZnO/Au/g-C₃N₄ film photocatalyst for reduction of CO₂ to CO, Appl. Catal. B: Environ. 283 (2021) 119638.

[42] L. Wang, Y. Feng, K. Wang, G. Liu, Solar water sterilization enabled by photothermal nanomaterials, Nano Energy 87 (2021), 106158.

[43] Y. Fu, L. Yang, J. Zhang, J. Hu, G. Duan, X. Liu, Y. Li, Z. Gu, Polydopamine antibacterial materials, Mater. Horiz. 8 (2021) 1618–1633.

[44] C. Mao, Y. Xiang, X. Liu, Y. Zheng, K.W.K. Yeung, Z. Cui, X. Yang, Z. Li, Y. Liang, S. Zhu, S. Wu, Local photothermal/photodynamic synergistic therapy by disrupting bacterial membrane to accelerate reactive oxygen species permeation and protein leakage, ACS Appl. Mater. Interfaces 11 (2019) 17902–17914.

[45] Z. Tang, R. Yin, W. Qu, H. Liu, H. Luo, D. Xia, Y. Huang, L. Shu, C. He, Flower pollen-based photosensitization process for enhanced solar disinfection of drinking water: reactor design and inactivation mechanisms, ACS EST Eng. 2 (2022) 629–641.

[46] O.K. Dalrymple, E. Stefanakos, M.A. Trotz, D.Y. Goswami, A review of the mechanisms and modeling of photocatalytic disinfection, Appl. Catal. B: Environ. 98 (2010) 27–38.

[47] D. Xia, Z. Tang, Y. Wang, R. Yin, H. He, X. Xie, J. Sun, C. He, P.K. Wong, G. Zhang, Piezo-catalytic persulfate activation system for water advanced disinfection: Process efficiency and inactivation mechanisms, Chem. Eng. J. 400 (2020), 125894.

[48] H. Sun, G. Li, X. Nie, H. Shi, P.K. Wong, H. Zhao, T. An, Systematic approach to in-depth understanding of photoelectrocatalytic bacterial inactivation mechanisms by tracking the decomposed building blocks, Environ. Sci. Technol. 48 (2014) 9412–9419.

[49] Y. Chong, C. Ge, G. Fang, R. Wu, H. Zhang, Z. Chai, C. Chen, J.J. Yin, Light-enhanced antibacterial activity of graphene oxide, mainly via accelerated electron transfer, Environ. Sci. Technol. 51 (2017) 10154–10161.

[50] G. Wang, K. Tang, Z. Meng, P. Liu, S. Mo, B. Mehrjou, H. Wang, X. Liu, Z. Wu, P. K. Chu, A quantitative bacteria monitoring and killing platform based on electron transfer from bacteria to a semiconductor, Adv. Mater. 32 (2020), e2003616.

[51] T. Wu, G. Liu, J. Zhao, H. Hidaka, N. Serpone, Evidence for H₂O₂ generation during the TiO₂-assisted photodegradation of dyes in aqueous dispersions under visible light illumination, J. Phys. Chem. B 103 (1999) 4862–4867.

[52] M. Kou, Y. Wang, Y. Xu, L. Ye, Y. Huang, B. Jia, H. Li, J. Ren, Y. Deng, J. Chen, Y. Zhou, K. Lei, L. Wang, W. Liu, H. Huang, T. Ma, Molecularly engineered covalent organic frameworks for hydrogen peroxide photosynthesis, Angew. Chem. Int. Ed. 61 (2022), e202200413.

[53] J. Hu, S. Wang, J. Yu, W. Nie, J. Sun, S. Wang, Duet Fe₃C and FeNₓ sites for H₂O₂ generation and activation toward enhanced electro-fenton performance in wastewater treatment, Environ. Sci. Technol. 55 (2021) 1260–1269.

[54] Y. Shiraishi, M. Matsumoto, S. Ichikawa, S. Tanaka, T. Hirai, Polythiophene-doped resorcinol-formaldehyde resin photocatalysts for solar-to-hydrogen peroxide energy conversion, J. Am. Chem. Soc. 143 (2021) 12590–12599.

[55] L. Jiang, X. Yuan, G. Zeng, J. Liang, X. Chen, H. Yu, H. Wang, Z. Wu, J. Zhang, T. Xiong, In-situ synthesis of direct solid-state dual Z-scheme WO_3/g-C_3N_4/Bi_2O_3 photocatalyst for the degradation of refractory pollutant, Appl. Catal. B: Environ. 227 (2018) 376–385.

[56] Y. Hong, Y. Jiang, C. Li, W. Fan, X. Yan, M. Yan, W. Shi, In-situ synthesis of direct solid-state Z-scheme V_2O_5/g-C_3N_4 heterojunctions with enhanced visible light efficiency in photocatalytic degradation of pollutants, Appl. Catal. B: Environ. 180 (2016) 663–673.

[57] L. Chen, M. Tang, C. Chen, M. Chen, K. Luo, J. Xu, D. Zhou, F. Wu, Efficient bacterial inactivation by transition metal catalyzed auto-oxidation of sulfite, Environ. Sci. Technol. 51 (2017) 12663–12671.

[58] D. Liu, W. Yao, J. Wang, Y. Liu, M. Zhang, Y. Zhu, Enhanced visible light photocatalytic performance of a novel heterostructured $Bi_4O_5Br_2$/$Bi_{24}O_{31}Br_{10}$/Bi_2SiO_5 photocatalyst, Appl. Catal. B: Environ. 172–173 (2015) 100–107.

[59] H. Lu, Q. Hao, T. Chen, L. Zhang, D. Chen, C. Ma, W. Yao, Y. Zhu, A high-performance Bi_2O_3/Bi_2SiO_5 p-n heterojunction photocatalyst induced by phase transition of Bi_2O_3, Appl. Catal. B: Environ. 237 (2018) 59–67.

[60] W. Xu, W. Tian, L. Meng, F. Cao, L. Li, Interfacial chemical bond-modulated Z-scheme charge transfer for efficient photoelectrochemical water splitting, Adv. Energy Mater. 11 (2021) 2003500.

[61] Q. Wang, D. Xu, Y. Dong, S. Pang, L. Zhang, G. Zhang, L. Lv, X. Liu, Y. Xia, L. C. Campos, Z. Ren, P. Wang, Unsaturated Nd-Bi dual-metal sites enable efficient NIR light-driven O_2 activation for water purification, Appl. Catal. B: Environ. 319 (2022), 121864.

[62] L. Qin, C.H. Huang, L. Mao, B. Shao, B.Z. Zhu, First unequivocal identification of the critical acyl radicals from the anti-tuberculosis drug isoniazid and its hydrazide analogs by complementary applications of ESR spin-trapping and HPLC/MS methods, Free Radic. Biol. Med. 154 (2020) 1–8.

[63] J. Demarteau, A. Debuigne, C. Detrembleur, Organocobalt complexes as sources of carbon-centered radicals for organic and polymer chemistries, Chem. Rev. 119 (2019) 6906–6955.

[64] Q. Lian, L. Hu, D. Ma, Y. Jiao, D. Xia, Y. Huang, Z. Tang, W. Qu, H. Zhao, C. He, D. D. Gang, Interstitial atomic Bi charge-alternating processor boosts twofold molecular oxygen activation enabling rapid catalytic oxidation reactions at room temperature, Adv. Funct. Mater. 32 (2022) 2205054.

[65] Q. Lian, A. Roy, O. Kizilkaya, D.D. Gang, W. Holmes, M.E. Zappi, X. Zhang, H. Yao, Uniform mesoporous amorphous cobalt-inherent silicon oxide as a highly active heterogeneous catalyst in the activation of peroxymonosulfate for rapid oxidation of 2,4-Dichlorophenol: the important role of inherent cobalt in the catalytic mechanism, ACS Appl. Mater. Interfaces 12 (2020) 57190–57206.

[66] L. Nie, D. Mei, H. Xiong, B. Peng, Z. Ren, X.I.P. Hernandez, A. DeLaRiva, M. Wang, M.H. Engelhard, L. Kovarik, A.K. Datye, Y. Wang, Activation of surface lattice oxygen in single-atom Pt/CeO_2 for low-temperature CO oxidation, Science 358 (2017) 1419–1423.

[67] H. Rabl, D. Wielend, S. Tekoglu, H. Seelajaroen, H. Neugebauer, N. Heitzmann, D. H. Apaydin, M.C. Scharber, N.S. Sariciftci, Are polyaniline and polypyrrole electrocatalysts for oxygen (O_2) reduction to hydrogen peroxide (H_2O_2)? ACS Appl. Energy Mater. 3 (2020) 10611–10618.

[68] H. Huang, C. Han, G. Wang, C. Feng, Lignin combined with polypyrrole as a renewable cathode material for H_2O_2 generation and its application in the electro-Fenton process for azo dye removal, Electrochim. Acta 259 (2018) 637–646.